Energy-based drag decomposition analyses for a turbulent channel flow developing over convergent–divergent riblets

Tongbiao Guo, Jian Fang, Shan Zhong, and Charles Moulinec

Published version information

Citation: T Guo et al. Energy-based drag decomposition analyses for a turbulent channel flow developing over convergent–divergent riblets. Phys Fluids 34, no. 2 (2022): 025115

DOI: 10.1063/5.0080867

Physics of Fluids

Energy-based drag decomposition analyses for a turbulent channel flow developing over convergent–divergent riblets

Cite as: Phys. Fluids **34**, 025115 (2022); https://doi.org/10.1063/5.0080867
Submitted: 04 December 2021 • Accepted: 25 January 2022 • Published Online: 10 February 2022

Tongbiao Guo (郭同彪), Jian Fang (方剑), Shan Zhong (钟山), et al.

Physics of Fluids ARTICLE scitation.org/journal/phf

Energy-based drag decomposition analyses for a turbulent channel flow developing over convergent–divergent riblets

Cite as: Phys. Fluids **34**, 025115 (2022); doi: 10.1063/5.0080867
Submitted: 4 December 2021 · Accepted: 25 January 2022 ·
Published Online: 10 February 2022

Tongbiao Guo (郭同彪),[1,2,a)] Jian Fang (方剑),[3] Shan Zhong (钟山),[1] and Charles Moulinec[3]

AFFILIATIONS

[1]School of Engineering, University of Manchester, Manchester M13 9PL, United Kingdom
[2]LHD, Institute of Mechanics, Chinese Academy of Sciences, Beijing 100190, China
[3]Scientific Computing Department, STFC Daresbury Laboratory, Warrington WA4 4AD, United Kingdom

[a)]Author to whom correspondence should be addressed: guotongbiao@imech.ac.cn

ABSTRACT

Direct numerical simulations of a turbulent channel flow developing over convergent–divergent (C–D) riblets are performed at a Reynolds number of $Re_b = 2800$, based on the half channel height δ and the bulk velocity. To gain an in-depth understanding of the origin of the drag generated by C–D riblets, a drag decomposition method is derived from kinetic energy principle for a turbulent channel flow with wall roughness. C–D riblets with a wavelength, Λ, ranging from 0.25δ to 1.5δ, are examined to understand the influence of secondary flow motions on the drag. It is found that as Λ increases, the intensity of the secondary flow motion increases first and then decreases, peaking at $\Lambda/\delta = 1$. At $\Lambda/\delta \geq 1$, some heterogeneity appears in the spanwise direction for the turbulent kinetic energy (TKE) and vortical structures, with the strongest enhancement occurring around regions of upwelling. All the riblet cases examined here exhibit an increased drag compared to the smooth wall case. From the energy dissipation/production point of view, such a drag increase is dominated by the TKE production and the viscous dissipation wake component. While the drag contribution from the TKE production shear component decreases as Λ increases, the drag contribution from the wake component of both the TKE production and viscous dissipation follows the same trend as the intensity of the secondary flow motion. From the work point of view, the drag increase in the riblet case at $\Lambda/\delta = 0.25$ comes mainly from the work of the Reynolds shear stresses, whereas at $\Lambda/\delta \geq 1$, the drag augmentation is dominated by the work of the dispersive stresses. At $\Lambda/\delta = 0.5$, both components play an important role in the increase in the drag, which also exhibits a peak.

I. INTRODUCTION

Convergent–divergent (C–D) riblets are composed of sections of left- and right-tilted grooves arranged in an alternating manner in the spanwise direction (see Fig. 1). They are a type of spanwise heterogeneous roughness patterns, which mimic the surface structures found on sharks' skin[1] and on the secondary flight bird feathers.[2] C–D riblets have received an increasing amount of research attention in recent years,[3–7] and they have been found to be capable of mitigating flow separation.[8,9]

C–D riblets were first studied experimentally by Koeltzsch *et al.*[1] in a turbulent pipe flow. They were found to cause spanwise variations of the streamwise velocity in the circumferential direction. Nugroho *et al.*[10] observed time-averaged large-scale secondary flow motions (roll modes) in the cross-stream plane over the ribleted strips, by using hot-wire measurement in a turbulent boundary layer flow. The secondary flow motions led to a spanwise variation in the boundary layer, with a thinner/thicker boundary layer occurring in regions of downwelling/upwelling. Kevin *et al.*[5] investigated the behavior of coherent structures using large field of view particle image velocimetry (LF-PIV) technique in a turbulent boundary layer developing over C–D riblets. Their results revealed that the mean large-scale roll modes were a time-averaged artifact of the unsteady and spanwise asymmetric secondary flow motions.

Quan *et al.*[8] applied an array of ribleted strips near the leading edge of a double ramp. They showed that the C–D riblets could mitigate shock-induced flow separation in a Mach 5 freestream. Investigating an array of C–D riblets fitted on the suction surface of diffuser blades in a linear cascade, the experimental results from Liu *et al.*[9] showed a reduction in up to 36.4% in the pressure loss coefficient. These researchers attributed the control effect to the momentum mixing induced by the large-scale roll mode generated by C–D riblets.

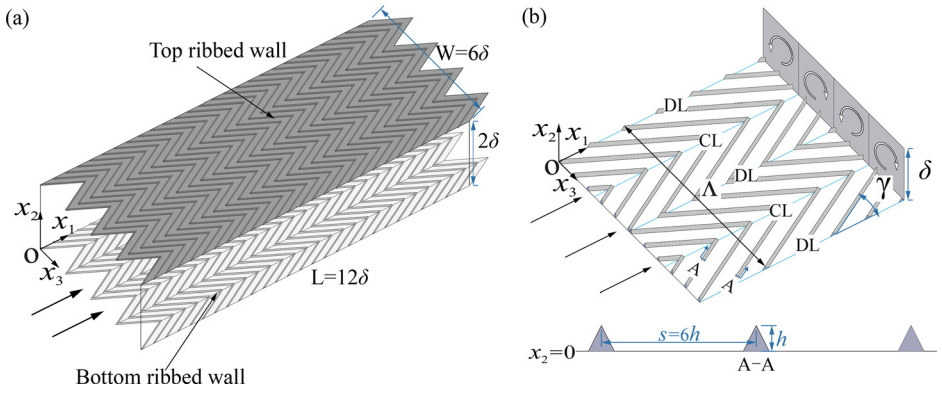

FIG. 1. (a) Computational domain with C–D riblets mounted on the bottom and top walls of a channel showing the symmetry with respect to the channel center plane. (b) Zoom of the computational domain to show the geometry parameters. The layout here is for the riblet case with $\Lambda = 1.5\delta$.

Most the studies of C–D riblets so far have been focused on the characterization of the large-scale roll mode, i.e., characterizing its general behavior and impact on the boundary layer. Consequently, much less attention has been placed in understanding the underlying drag generation mechanisms. Benschop *et al.*[11] conducted a series of direct numerical simulations (DNSs) in a turbulent channel flow over C–D riblets at a Reynolds number of $Re_b = 2750$, based on the half channel height and the bulk velocity. They reported that using C–D riblets led to an increase in drag and attributed this to the enhanced momentum exchange caused by the large scale secondary flow motions. Guo *et al.*[12] undertook detailed numerical simulations of a fully developed laminar channel flow in which a section of C–D riblets was applied upstream of a backward-facing rounded ramp at a Reynolds number of $Re_b = 400$ based on the inlet channel height and the bulk velocity. They found that a stronger roll mode not only led to a greater control effect but also was accompanied by a greater pressure loss or drag. This calls for further research in order to understand the underlying drag generation mechanisms induced by C–D riblets, and the role of the large scale secondary flow motions on the drag characteristics.

As a wall property, drag is commonly calculated via an integration of surface pressure and shear stress distributions. It is also known that statistical turbulence quantities play an important role in drag generation.[13,14] Fukagata *et al.*[15] proposed a momentum-based method to establish an explicit relation between drag coefficient and spatial distributions of Reynolds shear stresses for smooth-wall flows (denoted as the FIK method). This drag decomposition method has been applied to examine a number of flow control methods, including opposition control,[15] uniform wall blowing/suction,[16] alternation of the slip boundary condition,[17] and spanwise wall oscillation.[18] It provides some new insights of the physical mechanisms of drag generation in the respective flows. An alternative drag decomposition method based on energy balance was proposed by Renard and Deck.[19] They decomposed the skin friction for wall-bounded flows into the contributions of molecular viscous dissipation, production of turbulent kinetic energy (TKE) and spatial growth of the flow (denoted as the RD method). They used this method to explore the influence of the Reynolds number on mean skin friction generation. They found that while the skin friction at high Reynolds numbers was dominated by TKE production within the logarithmic layer, the buffer-layer dynamics played a dominant role at low Reynolds numbers. Li *et al.*[20] extended this method to analyze the effect of compressibility on drag.

The original FIK and RD methods were developed for analyzing smooth-wall flows. Peet and Sagaut[21] extended the FIK method to allow homogeneous surfaces of any shape, where the drag is decomposed into bulk, asymmetric, pressure, transient, and turbulent contributions. They used this method to analyze the influence of different dynamic effects on a skin friction modification by longitudinal riblets. Recently, Nikora *et al.*[22] extended the FIK method to study open-channel flows with spanwise heterogeneous roughness patterns, whereby the drag is divided into the contributions of viscous, Reynolds, and dispersive stresses, respectively. They found that, as the Reynolds number increased, while the drag contribution of the viscous stresses reduced sharply, the dispersive and Reynolds stresses continued to play a dominant role in drag generation. In their method, an additional parameter N, which is related to roughness shape/size, wall shear stress, and the so-called drag length scale and depth-roughness length scale, was introduced to characterize the flow-rough-bed interactions. Setting up N is not a straightforward task,[22] especially because its value depends on the roughness pattern. This motivates the need for the derivation of a universal drag decomposition method.

In this paper, the original RD method is extended for the first time to a turbulent flow in a channel with wall roughness. The drag coefficient is decomposed into physics-informed contributions from several flow field moments without inclusion of any additional parameter. The flow field data used in our drag analyses are produced by DNSs of a turbulent channel flow over C–D riblets at a Reynolds number of $Re_b = 2800$ based on the half channel height δ and the bulk velocity. C–D riblets with a wavelength of 0.25δ–1.5δ are investigated in order to introduce secondary flow motions with different scales and strengths to the flow. Two drag expressions, based on the drag decomposition method, are derived and applied to gain an in-depth understanding of the origin of the drag generated by C–D riblets. One expression is based on energy dissipation/production considerations, whereby the drag contributions from the viscous dissipation at the wall-normal plane-averaged and wake level as well as the turbulent production are looked at; the other one is based on the work point of view, whereby the drag is decomposed into contributions from the work done by the viscous and pressure forces, the Reynolds shear stresses and the dispersive stress, respectively. The objectives of this study are twofold: (1) to propose a new energy-based drag decomposition method, which can be used to analyze the drag in a turbulent channel flow developing over wall roughness and (2) to provide an

TABLE I. Computational domain size and mesh distributions for all the DNS cases. The superscript "+" denotes the variables in wall units, calculated from the wall friction velocity of the baseline case (U_τ).

Case	Re_b	Re_τ	L/δ	W/δ	Λ/δ	N_{x_1}	N_{x_2}	N_{x_3}	Δx_1^+	Δx_2^+	Δx_3^+
Baseline	2800	180	12	6		216	154	270	10	0.3–4	4
Riblet	2800		12	6	0.25,0.5,1,1.5	2160	154	560	1	0.1–4	1.9

insight of the drag generation mechanism of C–D riblets by identifying the role that the secondary flow plays in drag generation.

II. METHODOLOGY

A. C–D riblet parameters

The computational domain of the turbulent channel flow is shown in Fig. 1(a) with the local enlarged drawing shown in Fig. 1(b). C–D riblets are mounted to the bottom and top walls, and they are symmetrical with respect to the channel center plane. The streamwise, wall-normal, and spanwise directions of the coordinate system are denoted by x_1, x_2, and x_3, respectively, and the corresponding velocity components are u_1, u_2, and u_3. The computational domain size is the same for all the cases with the streamwise length $L = 12\delta$, the channel height $H = 2\delta$, and the spanwise width $W = 6\delta$, where δ is half of the channel height.

C–D riblets are made of strips of left- and right-tilted grooves in the spanwise direction. From the view of the incoming flow, the streamwise line adjacent to the ribleted strips diverges away from the diverging line (DL), while the lines adjacent to the strips tend to converge toward each other. It is called the converging line (CL) and shown in Fig. 1(b). The angle that the riblet passage forms with the x_1-axis is referred to as the yaw angle γ. In this paper, γ is set to 30° for all the riblet cases. The spanwise width of two adjacent DL or CL is the wavelength (Λ), and a parametric study of Λ is carried out in this paper with $\Lambda/\delta = 0.25$, 0.5, 1, and 1.5, respectively. Riblets with trapezoidal cross sections are used; the riblet height h, spacing s, and ridge angle α are $h = \delta/36$, $s = 6h$ and $\alpha = 53°$, respectively.

B. Numerical method

The in-house code ASTR[23–25] is used to perform all the direct numerical simulations. The three-dimensional unsteady Navier–Stokes equations in a non-dimensional form are solved numerically in a generalized coordinate system within the framework of the finite-difference method. The spatial derivatives are approximated using a sixth-order compact central scheme.[26] The second derivatives present in the diffusive terms are not directly calculated. The velocity components and temperature are differentiated first to express the stress tensor and the heat flux vector at each node point. The diffusion terms are then computed by applying a second time the finite-difference scheme on the stress and heat flux. After all the spatial terms are solved, an explicit time-scheme, which is the third-order three-stage Runge–Kutta method, is used for temporal integration.

Periodic boundary conditions are applied in the streamwise and side directions, while on the bottom and top wall, isothermal no-slip boundary conditions are enforced. A body force drives the flow in the streamwise direction with a constant flow rate. The mesh is made of hexahedral cells for the whole computational domain, and the number of grid points in each direction is shown in Table I for each case. The mesh topology is shown in Fig. 2(a), where the grid is plotted every tenth grid line in each direction. The mesh distribution of the near wall region in the longitudinal ($x_1 - x_2$) plane is further displayed in Fig. 2(b), where the mesh is orthogonal in the vicinity of the riblet grooves. The first grid point away from the wall is located within $x_2^+ \leq 0.3$, where x_2^+ is the non-dimensional distance from the wall to the first fluid grid point.

The bulk Reynolds number is defined as $Re_b = U_b\delta/\nu$, where U_b is the bulk velocity and ν is the kinematic viscosity of the fluid. For all the cases $Re_b = 2800$. The friction Reynolds number $Re_\tau = U_\tau\delta/\nu$, where U_τ is the friction velocity is set to $Re_\tau = 180$ for the baseline case without riblets. The Mach number based on the bulk velocity and speed of sound at the wall is 0.2. Therefore, the present research is restricted to a low Reynolds number and an incompressible regime. The riblet height and spacing scaled in wall units of the baseline case are $h^+ = hU_\tau/\nu = 5$ and $s^+ = sU_\tau/\nu = 30$, respectively.

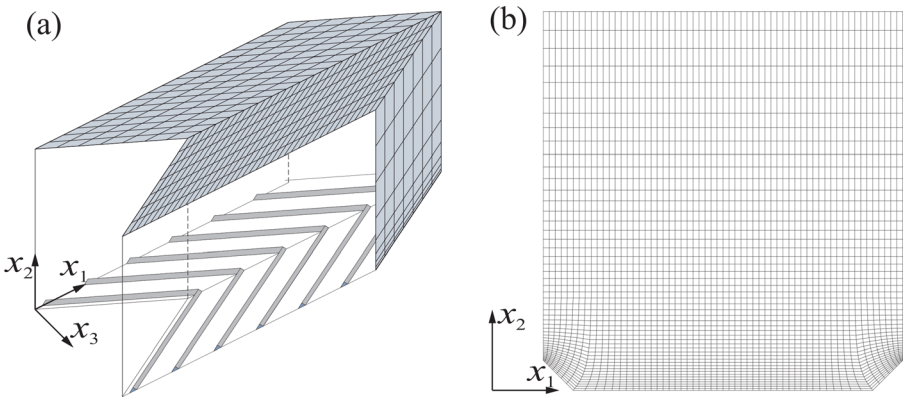

FIG. 2. (a) Snapshot of the computational domain with the mesh plotted every tenth grid line in each direction. (b) Mesh distribution near the bottom wall in the ($x_1 - x_2$) plane. The mesh is for the riblet case at $\Lambda = 1.5\delta$.

C. Averaging methodology

For the flows investigated in this paper, which are all incompressible, Reynolds averaging is applied. The ith instantaneous velocity component, u_i ($i = 1, 2, 3$), is written as $u_i = \bar{u}_i + u_i'$, where $\bar{u}_i$ is the time-averaged velocity and u_i' is the time-fluctuating component. The Reynolds stress tensor is expressed as $\overline{u_i'u_j'}$, and the TKE is $k = \frac{1}{2}\overline{u_i'u_i'}$. (Einstein notation is applied with summation on repeated indices.)

For the turbulent flow over roughness, the intrinsic spatial average[27] is conducted and denoted here by angle brackets,

$$\langle\Theta\rangle_{x_1}(x_2,x_3) = \frac{1}{\psi(x_2,x_3)L}\int_L \Theta(x_1,x_2,x_3)dx_1, \tag{1a}$$

$$\langle\Theta\rangle_{x_1x_3}(x_2) = \frac{1}{\phi(x_2)LW}\int\int_{LW} \Theta(x_1,x_2,x_3)dx_1dx_3, \tag{1b}$$

where Θ represents any variable, such as the mean velocity component $\bar{u}_i$; $\langle\cdot\rangle_{x_1}$ denotes the intrinsic average in the x_1 direction; $\langle\cdot\rangle_{x_1x_3}$ indicates averaging in the $(x_1 - x_3)$ plane (the subscript is omitted hereafter for simplicity); $\psi(x_2,x_3)$ is the ratio of length occupied by the fluid to the length (L) in the x_1-direction, while $\phi(x_2)$ is the ratio of area occupied by the fluid to the total area (LW) in the wall-parallel plane.

Based on the time- and space-average, a triple decomposition of the velocity is introduced,[28–30]

$$u_i(x_1,x_2,x_3,t) = \langle\bar{u}_i\rangle(x_2) + \tilde{\bar{u}}_i(x_1,x_2,x_3) + u_i'(x_1,x_2,x_3,t), \tag{2}$$

where $\tilde{\bar{u}}_i(x_1,x_2,x_3)$ denotes the dispersive velocity component (wake component) in the wall-parallel plane.

D. Validation of the computational method

To validate the present computational method, the profiles of the mean velocity and Reynolds stress (normalized by the friction velocity U_τ) in the baseline case without riblets are compared with the incompressible DNS data of Moser *et al.*[31] Figure 3 shows that the results between the present DNS and reported by Moser *et al.*[31] match very well. A closer examination of the Reynolds stress shows that the maximum difference is observed for the $\overline{u_i'u_j'}^+$ around the peak, and the corresponding error is less than 0.2%. It proves that the simulation method applied in this paper is adequate.

E. Grid-independence study

To ensure that the mesh resolution is sufficient for the flow field analysis, a grid-independence study is performed for the riblet case of $\Lambda/\delta = 0.5$. Three cases with coarse/medium/fine meshes are used with their mesh topology shown in Fig. 2. The mesh size and grid point number shown in Fig. 2 and Table I are given for the fine-mesh case. The grid size in the wall-normal direction is the same for the three cases, while in the other two directions, the grid size of the medium- and fine-meshes is twice and four times as that of the coarse-mesh case, respectively.

Figure 4 shows the profiles of the streamwise velocity as well as the turbulent kinetic energy k and Reynolds stress $-\overline{u_1'u_2'}$ in the riblet case at $\Lambda/\delta = 0.5$ with different mesh densities. As the mesh resolution increases, the profiles for the three different simulations tend to fall on top of each other, and the results for the medium-mesh and fine-mesh cases are very close to each other. The contours of the mean streamwise velocity with in-plane velocity vectors in the cross-stream plane of the lower half part of channel flow are displayed in Fig. 5. Here and hereafter, only one wavelength in the spanwise direction is drawn for clarity. Figure 5 shows that no distinguishable differences can be seen in the results between the medium- and fine-mesh cases. Therefore, the fine-mesh case's resolution is considered as being sufficient for all the simulations and is used to produce the results presented in the following flow analysis.

III. DRAG DECOMPOSITION IN A FULLY DEVELOPED FLOW IN A CHANNEL WITH WALL ROUGHNESS

In this section, the drag decomposition for a streamwise-periodic incompressible turbulent flow in a channel with periodic wall roughness is derived, based on the kinetic energy equation, under the following working conditions:

(A) constant flow rate in the streamwise direction,
(B) no-slip velocity at the wall,
(C) periodic roughness with respect to streamwise and side planes,
(D) symmetric roughness with respect to side planes.

As a result, the following relation is satisfied,

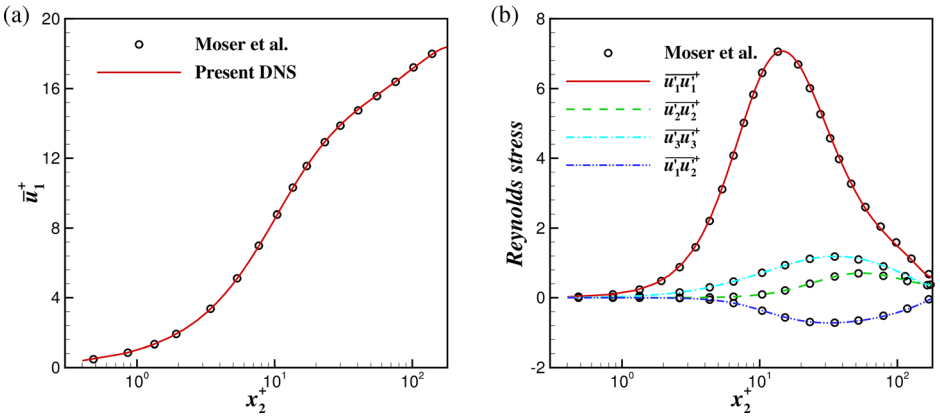

FIG. 3. Profiles of (a) the mean velocity and (b) Reynolds stress (normalized by U_τ) in the baseline case at $Re_b = 2800$ ($Re_\tau = 180$). $\bar{u}_1^+ = \bar{u}_1/U_\tau$, $x_2^+ = x_2U_\tau/\nu$, $\overline{u_i'u_j'}^+ = \overline{u_i'u_j'}/U_\tau^2$.

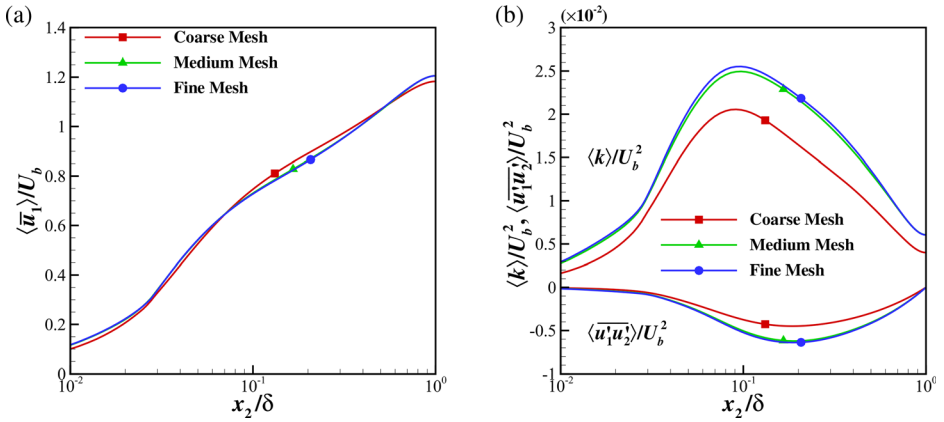

FIG. 4. Profiles of (a) the mean velocity and (b) turbulent kinetic energy k and Reynolds stress $-\overline{u_1'u_2'}$ in the riblet case of $\Lambda/\delta = 0.5$ with three different mesh densities.

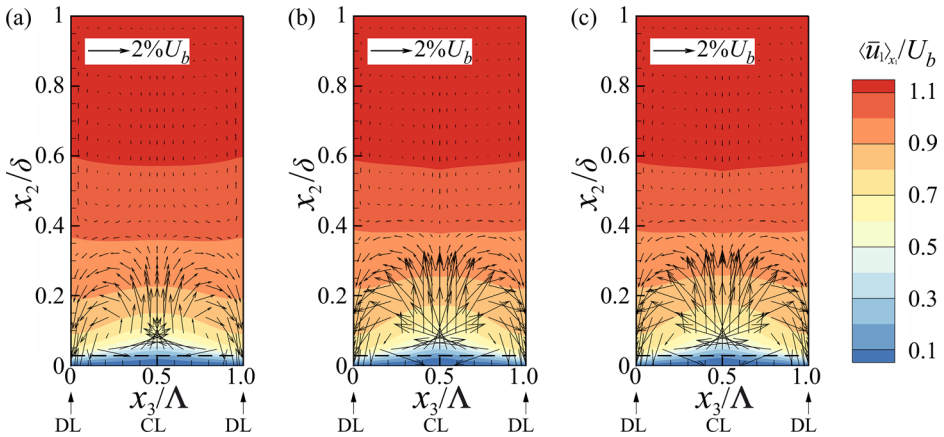

FIG. 5. Contours of the streamwise velocity superimposed with in-plane velocity vectors in cross-stream planes for the riblet case at $\Lambda/\delta = 0.5$ using the (a) coarse mesh, (b) medium mesh, and (c) fine mesh, respectively.

$$\frac{\partial\langle\bar{u}_i\rangle}{\partial x_1} = 0, \quad \frac{\partial\langle\bar{u}_i\rangle}{\partial x_3} = 0, \quad \langle\bar{u}_2\rangle = 0,$$
$$\langle\bar{u}_3\rangle = 0, \quad \frac{\partial\langle\bar{u}_i\rangle}{\partial x_i} = 0, \quad \frac{\partial\tilde{\bar{u}}_i}{\partial x_i} = 0, \tag{3}$$

where the continuity equation $\frac{\partial\bar{u}_i}{\partial x_i} = 0$ is applied; $\langle\bar{u}_2\rangle(x_2) = 0$ is obtained by integrating the continuity equation across the fluid domain below x_2 with the aid of the Gauss's Theorem.

The time-averaged momentum equation is expressed as

$$\frac{\partial\bar{u}_i}{\partial t} + \bar{u}_j\frac{\partial\bar{u}_i}{\partial x_j} = \frac{1}{\rho}\delta_{i1}\bar{f}_1 - \frac{1}{\rho}\frac{\partial\bar{p}}{\partial x_i} + \nu\frac{\partial}{\partial x_j}\left(\frac{\partial\bar{u}_i}{\partial x_j}\right) - \frac{\partial\overline{u_i'u_j'}}{\partial x_j}, \tag{4}$$

where ρ and p are the density and pressure of the flow, respectively; $\bar{f}_1$ denotes the uniform body force that drives the flow in the streamwise direction. For the present streamwise- and spanwise-periodic fully developed channel flows, $\frac{\partial\bar{u}_i}{\partial t}$ is zero. Multiplying this equation by $\bar{u}_i$ and rearranging some terms, the integral form of the transport equation for the mean kinetic energy per mass unit $K \equiv \bar{u}_i\bar{u}_i/2$ is expressed as

$$\int_{V_f}\frac{\partial}{\partial x_j}\left[\bar{u}_jK + \frac{\bar{u}_j\bar{p}}{\rho} + \bar{u}_i\overline{u_i'u_j'} - \nu\frac{\partial K}{\partial x_j}\right]dV$$
$$= \int_{V_f} -\nu\frac{\partial\bar{u}_i}{\partial x_j}\frac{\partial\bar{u}_i}{\partial x_j} + \overline{u_i'u_j'}\frac{\partial\bar{u}_i}{\partial x_j} + \frac{\bar{u}_1}{\rho}\bar{f}_1 dV, \tag{5}$$

where V_f is the volume of the fluid domain and the following equation has been applied:

$$\bar{u}_i\frac{\partial}{\partial x_j}\left(\frac{\partial\bar{u}_i}{\partial x_j}\right) = \frac{\partial}{\partial x_j}\left(\bar{u}_i\frac{\partial\bar{u}_i}{\partial x_j}\right) - \frac{\partial\bar{u}_i}{\partial x_j}\frac{\partial\bar{u}_i}{\partial x_j} = \frac{\partial}{\partial x_j}\left(\frac{\partial K}{\partial x_j}\right) - \frac{\partial\bar{u}_i}{\partial x_j}\frac{\partial\bar{u}_i}{\partial x_j}. \tag{6}$$

Using the assumption presented above and with the aid of the Gauss's Theorem, the left-hand side of Eq. (5) becomes

$$\int_{V_f}\frac{\partial}{\partial x_j}\left[\bar{u}_jK + \frac{\bar{u}_j\bar{p}}{\rho} + \bar{u}_i\overline{u_i'u_j'} - \nu\frac{\partial K}{\partial x_j}\right]dV$$
$$= \oint_{S_f}\left[\bar{u}_jK + \frac{\bar{u}_j\bar{p}}{\rho} + \bar{u}_i\overline{u_i'u_j'} - \nu\frac{\partial K}{\partial x_j}\right]n_j dS = 0, \tag{7}$$

where S_f denotes the surface enclosing the fluid domain and $\vec{n} = (n_1, n_2, n_3)$ is the outward-pointing unit normal at each point of the boundary surface. From the physics point of view, Eq. (7) indicates that convection and diffusion of the mean kinetic energy have no influence on its overall integral if the flow assumptions set in this work are considered.

Since the volume force is constant across the whole domain,

$$\int_{V_f}\bar{u}_1\bar{f}_1 dV = \bar{f}_1\int_{V_f}\bar{u}_1 dV = \bar{f}_1 V_f U_b. \tag{8}$$

As a result, Eq. (5) is expressed as

$$\frac{1}{\rho}\bar{f}_1 V_f U_b = \int_{V_f} \nu \frac{\partial \bar{u}_i}{\partial x_j}\frac{\partial \bar{u}_i}{\partial x_j} dV + \int_{V_f} -\overline{u_i' u_j'}\frac{\partial \bar{u}_i}{\partial x_j} dV. \quad (9)$$

Equation (9) is a power equation and can be interpreted as the energy balance of the mean motion. The term on the left-hand side represents the rate of work done by the body force in the fluid domain. It is balanced by two parts on the right-hand side: one directly dissipated by the mean flow and the other one converted into turbulent kinetic energy production, which is ultimately converted into internal energy via turbulent dissipation.

Integrating the x_1-momentum equation in Eq. (4) across the fluid domain and applying a similar method as displayed above with the aid of the Gauss's Theorem, leads to the following force balance in the x_1-direction for the present streamwise-periodic flow:

$$\bar{f}_1 V_f = F_{wall} = C_D 0.5 \rho U_b^2 A, \quad (10)$$

where C_D denotes the drag coefficient; $A = 2LW$ is the reference area; and F_{wall} represents the total drag force acting on the top and bottom wall, which can be obtained via wall surface integration of pressure and shear stress. By combining Eqs. (9) and (10), the drag coefficient C_D in a turbulent channel flow can be expressed as

$$C_D = \frac{1}{U_b^3 LW}\int_{V_f} \nu \frac{\partial \bar{u}_i}{\partial x_j}\frac{\partial \bar{u}_i}{\partial x_j} dV + \frac{1}{U_b^3 LW}\int_{V_f} (-\overline{u_i' u_j'})\frac{\partial \bar{u}_i}{\partial x_j} dV. \quad (11)$$

For wall roughness that are symmetrical with respect to the channel center plane (e.g., C–D riblets), the drag coefficient in Eq. (11) can be calculated using the lower half part of the channel flow. By applying the wall-parallel plane average defined in Eq. (1b), Eq. (11) reads

$$C_D = \frac{2}{U_b^3}\int_0^\delta \nu \left\langle \frac{\partial \bar{u}_i}{\partial x_j}\frac{\partial \bar{u}_i}{\partial x_j} \right\rangle dx_2 + \frac{2}{U_b^3}\int_0^\delta \left\langle -\overline{u_i' u_j'}\frac{\partial \bar{u}_i}{\partial x_j} \right\rangle dx_2. \quad (12)$$

Equation (12) provides an alternative way to calculate the drag coefficient. In comparison with the conventional methods, which rely on wall surface integration of the tangential and normal forces, the present method provides more detailed information about the location and physical parameters of the energy losses. It is expected to lead to a new understanding of the drag characteristics by extracting more information from the flow field.

For the fully developed flow in a channel with smooth wall, the drag coefficient becomes

$$C_D = \frac{2}{U_b^3}\int_0^\delta \nu \left(\frac{\partial \bar{u}_1}{\partial x_2}\right)^2 dx_2 + \frac{2}{U_b^3}\int_0^\delta (-\overline{u_1' u_2'})\frac{\partial \bar{u}_1}{\partial x_2} dx_2. \quad (13)$$

IV. RESULTS AND DISCUSSION

In this section, the influence of the C–D riblets on the mean velocity field and turbulent structures is examined first. Then, the drag characteristics are analyzed from two perspectives, using the proposed drag decomposition method.

A. Flow characteristics

The contours of the mean streamwise velocity with in-plane velocity vectors in the cross-stream plane of the lower half part of the channel flow are displayed in Fig. 6. Contours of the streamwise velocity in the baseline case are also provided in Fig. 6(e) for comparison. All contours presented in this paper are shown with streamwise averaging, defined in Eq. (1a). For all the riblet cases, secondary flow motions characterized by rotating vortices are observed, with an downward/upward motion achieved around the DL/CL. This is consistent with the stereoscopic particle image velocimetry experiments of Kevin *et al.*[3] and Xu *et al.*,[32] carried out in the turbulent boundary layer flow developing over C–D riblets.

The spanwise velocity near the riblet valleys induced by the yawed grooves acts as the driving force for the rotating vortices in the cross-stream plane. To satisfy mass conservation, a downward and upward motion occurs near the DL and CL, respectively. For the riblet case at $\Lambda/\delta = 0.25$, there is not enough spanwise space to enable the development of the spanwise velocity between the longitudinal planes over the DL and CL [see Fig. 8(a)], where the spanwise velocity is zero because of the geometric symmetry. Consequently, the intensity of the secondary roll mode is relatively weak, and confined in the near wall region, its vortex center being located below $x_2/\delta = 0.05$. As the wavelength increases, there is a growing space for the spanwise velocity [see Fig. 8(a)] to increase and the roll motion to develop. The size and intensity of the secondary roll motion tend to increase, and the vortex center moves gradually further away from the wall. The upward motion around the CL takes the low-momentum fluid away from the wall, leading to the low velocity region nearby. In contrast, the downward motion transports the high-speed fluid toward the wall and contributes to the increase in the velocity. As a result, a variation of the streamwise velocity in the spanwise direction is observed with increasing/decreasing velocity observed around the DL/CL, respectively.

Figure 7 presents the contours of the mean streamwise vorticity Ω_1 along with in-plane velocity vectors in the cross-stream plane. For each riblet case, large secondary flows characterized by a pair of wavelength-scale counter-rotating vortices are observed above the riblet crests. For the riblet case at $\Lambda/\delta = 0.25$, the region with high magnitude of Ω_1 is confined below $x_2/\delta = 0.15$, while at $\Lambda/\delta = 1.0$ and 1.5, the region is up to $x_2/\delta = 0.3$, owing to the increased spanwise space to enable Ω_1 to develop between DL and CL. Figure 8(a) shows that the magnitude of $\bar{u}_3$ (average in the wall-normal plane from $x_3/\Lambda = 0$ to $x_3/\Lambda = 0.5$) reaches its maximum around $x_2/\delta = 0.02$, where the sign of $\frac{\partial \bar{u}_3}{\partial x_2}$ changes. $\frac{\partial \bar{u}_3}{\partial x_2}$ is the main contributor of Ω_1, and the induced sign of Ω_1 below the riblet crests is opposite to that above the riblet crests.

The strength of the secondary flows generated by the C–D riblets is quantified by integrating $|\Omega_1|$ and $\sqrt{\bar{u}_2^2 + \bar{u}_3^2}$ across the fluid domain, namely,

$$\Gamma_1 = \frac{1}{V_f}\int_{V_f} \sqrt{\bar{u}_2^2 + \bar{u}_3^2}/U_b \, dV, \quad (14a)$$

$$\Gamma_2 = \frac{1}{V_f}\int_{V_f} |\Omega_1|\delta/U_b \, dV. \quad (14b)$$

Figure 8(b) shows that both Γ_1 and Γ_2 increase initially with Λ to a maximum and then decrease, peaking at $\Lambda/\delta = 1$. This finding is consistent with that in ridge- and strip-type spanwise heterogeneous roughness patterns observed by Vanderwel *et al.*,[33] Chung *et al.*,[34] and Wang *et al.*[35] In their studies, they found that the large-scale roll motion is most pronounced when the spanwise wavelength equals

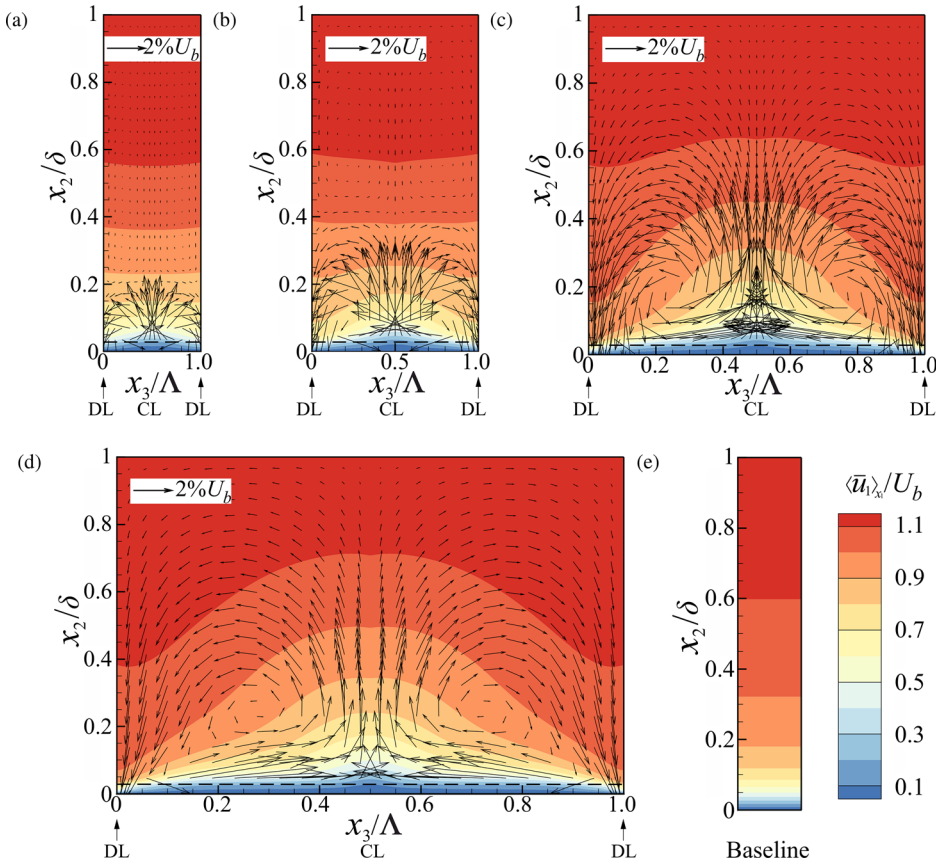

FIG. 6. Contours of streamwise velocity superimposed with in-plane velocity vectors in cross-stream planes for riblet cases with (a) $\Lambda/\delta = 0.25$, (b) $\Lambda/\delta = 0.5$, (c) $\Lambda/\delta = 1$, and (d) $\Lambda/\delta = 1.5$, and (e) baseline case. The dashed line denotes the vertical position of the riblet crest.

approximately to the characteristic length scale (e.g., boundary layer thickness in boundary layer flows). Note that the roll motion induced by these two roughness patterns belongs to the secondary flow of Prandtl's second kind, produced by turbulence heterogeneity.[36] In contrast, the roll motion induced by the C–D riblets comes from the yawed grooves that drive the near-wall fluid deviating away from the streamwise direction, belonging to the secondary flow of Prandtl's first kind (also known as geometry-driven secondary flow). For each kind

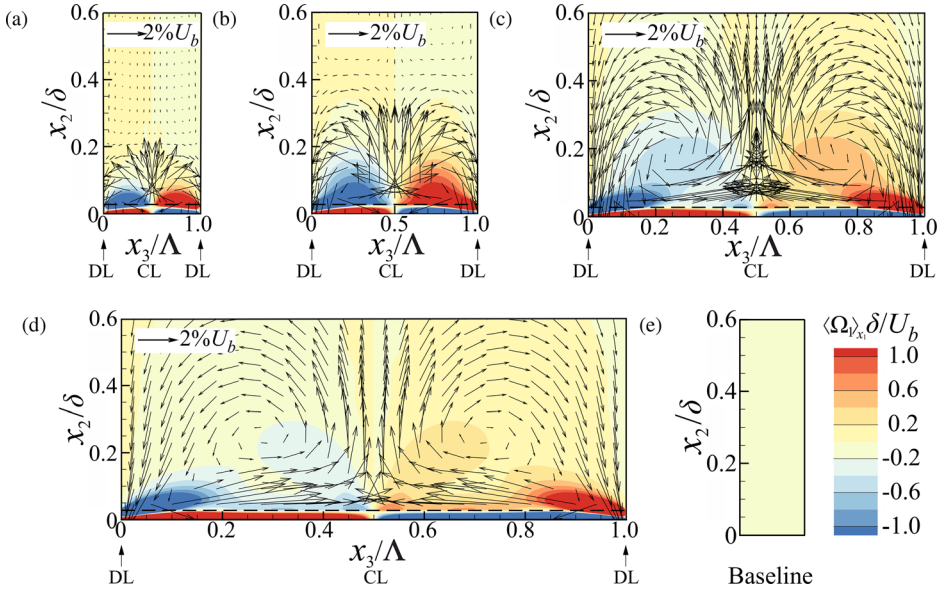

FIG. 7. Contours of streamwise vorticity superimposed with in-plane velocity vectors in cross-stream planes for riblet cases with (a) $\Lambda/\delta = 0.25$, (b) $\Lambda/\delta = 0.5$, (c) $\Lambda/\delta = 1$, and (d) $\Lambda/\delta = 1.5$, and (e) baseline case. The dashed line denotes the vertical position of the riblet crest.

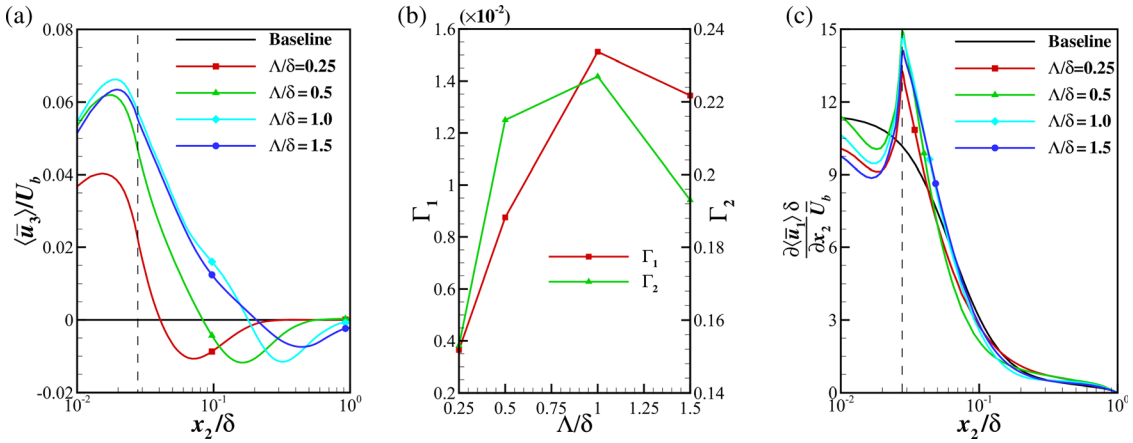

FIG. 8. (a) Profile of the wall-normal plane-averaged (within half wavelength from $x_3/\Lambda = 0$ to $x_3/\Lambda = 0.5$) spanwise velocity. (b) Variations of Γ_1 and Γ_2 with an increasing riblet wavelength. (c) Profile of the wall-normal plane-averaged mean velocity gradient $\frac{\partial \langle \bar{u}_1 \rangle}{\partial x_2}$. The vertical dashed line denotes the position of riblet crest.

of roughness patterns, the evolution of the intensity of the roll motion follows the same variation trend as the spanwise wavelength.

The mean velocity gradient $\frac{\partial \langle \bar{u}_1 \rangle}{\partial x_2}$ is shown in Fig. 8(c). Compared with the baseline case, the main difference for $\frac{\partial \langle \bar{u}_1 \rangle}{\partial x_2}$ for the riblet cases appears around the riblet crest where $\frac{\partial \langle \bar{u}_1 \rangle}{\partial x_2}$ peaks and shows an increase.

B. Turbulent structures

The influence of the C–D riblets on the instantaneous turbulent structures is examined, using the λ_{ci}-criterion.[37] Figure 9 displays the instantaneous iso-surfaces of swirling strength λ_{ci}, colored by the positive (red color) and negative (blue color) streamwise vorticity ω_1 for the different cases. In comparison with the baseline case, a significantly increased number of vortical structures is observed in all the riblets cases, despite the small riblet height with $h^+ = 5$, the vortex amplification decreasing as the wavelength increases. For the riblet case at $\Lambda/\delta = 0.25$, the instantaneous structures with positive and negative vorticity seem to randomly distribute across the channel. In contrast, at $\Lambda/\delta = 1.5$, some heterogeneity is observed for the turbulent structures in the spanwise direction, these structures being concentrated around the upwelling region. This can be attributed to the accumulation of the near-wall turbulence-rich fluid and its upward motion. Similar results have been found in flows with large-scale roll mode induced by ridge-type spanwise heterogeneous surface pattern,[28] active wall actuation,[25] and C–D riblets with spanwise-varied riblet height.[11]

The strong instantaneous vortical structures contribute to the increase in turbulent kinetic energy k. As a result, for the riblet cases at $\Lambda/\delta = 0.25$ and $\Lambda/\delta = 0.5$, k exhibits a substantial increase across the whole span, as observed by comparing Figs. 9(b) and 9(c) and 10(b) and 10(c). As the wavelength increases to $\Lambda/\delta = 1.5$, the enhancement of k occurs mainly around the converging region with a reduction in a narrow vertical region near the diverging line. Such a spanwise heterogeneity of k is due to the downwelling and upwelling generated by the large-scale secondary flow. This is different from the flow over homogeneous roughness where no large-scale secondary flow is produced and where the heterogeneity is only present in the vicinity of the rough wall.[38]

C. Drag analysis using the drag decomposition method

In this section, the drag characteristics are analyzed based on the proposed drag decomposition method given in Eq. (12), where the drag coefficient C_D is decomposed into $C_{D,v}$ and $C_{D,k}$, resulting from the time-averaged viscous dissipation and turbulent production. C_D and its two components are shown in Fig. 11(a) for all the cases. The difference observed in the drag coefficient between the results using Eq. (12), and the conventional method via the wall surface integration of the pressure and shear stress is also presented. A comparison shows an error of less than 1%. Compared to the baseline case, C_D, $C_{D,v}$, and $C_{D,k}$ for the riblet cases are significantly higher, and C_D peaks at $\Lambda/\delta = 0.5$. As the wavelength increases, while $C_{D,v}$ follows the same variation trend as Γ with the peak at $\Lambda/\delta = 1$, $C_{D,k}$ shows a decreasing trend.

In order to better understand the mechanism of drag augmentation induced by C–D riblets, a further decomposition of the drag coefficient is performed, based on the triple decomposition of the velocity given in Eq. (2). Substituting Eq. (2) into Eq. (12) gives

$$
\begin{aligned}
C_D = {} & \underbrace{\frac{2}{U_b^3}\int_0^\delta \phi \underbrace{\nu \frac{\partial \langle \bar{u}_1 \rangle}{\partial x_2}\frac{\partial \langle \bar{u}_1 \rangle}{\partial x_2}}_{\langle v_a \rangle} dx_2}_{C_{D,va}} + \underbrace{\frac{2}{U_b^3}\int_0^\delta \phi \underbrace{\nu \left\langle \frac{\partial \tilde{\bar{u}}_i}{\partial x_j}\frac{\partial \tilde{\bar{u}}_i}{\partial x_j} \right\rangle}_{\langle v_d \rangle} dx_2}_{C_{D,vd}} \\
& + \underbrace{\frac{2}{U_b^3}\int_0^\delta \phi \underbrace{2\nu \frac{\partial \langle \bar{u}_1 \rangle}{\partial x_2}\left\langle \frac{\partial \tilde{\bar{u}}_1}{\partial x_2} \right\rangle}_{\langle v_i \rangle} dx_2}_{C_{D,vi}} + \underbrace{\frac{2}{U_b^3}\int_0^\delta \phi \underbrace{\langle -\overline{u_1' u_2'} \rangle \frac{\partial \langle \bar{u}_1 \rangle}{\partial x_2}}_{\langle P_{ks} \rangle} dx_2}_{C_{D,ks}} \\
& + \underbrace{\frac{2}{U_b^3}\int_0^\delta \phi \underbrace{\left\langle -\overline{u_i' u_j'} \frac{\partial \tilde{\bar{u}}_i}{\partial x_j} \right\rangle}_{\langle P_{kw} \rangle} dx_2}_{C_{D,kw}},
\end{aligned}
\tag{15}
$$

where $C_{D,v}$ is decomposed into $C_{D,va}$, $C_{D,vd}$, and $C_{D,vi}$, denoting the contribution from the viscous dissipation at the wall-normal

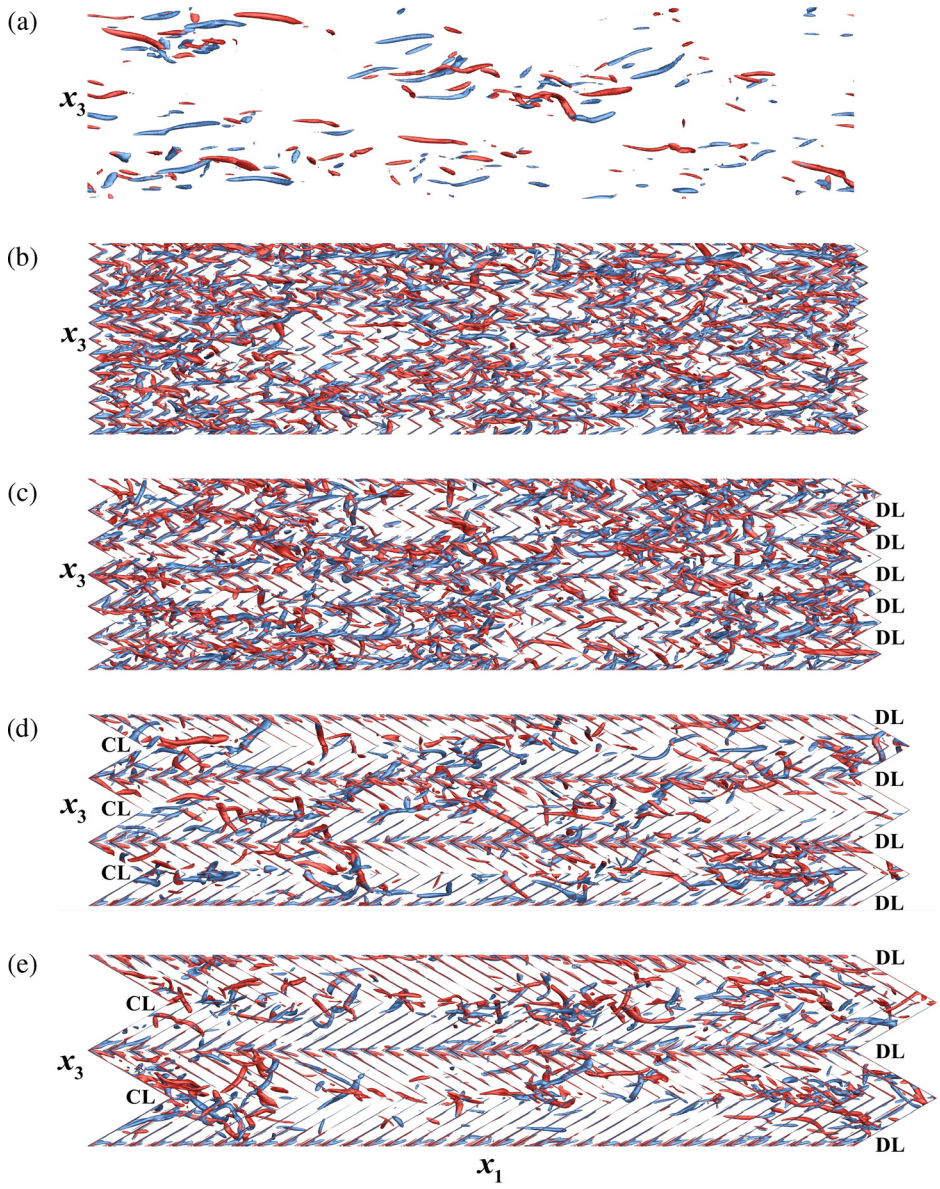

FIG. 9. Iso-surfaces of the swirling strength λ_{ci} for (a) the baseline case with $\lambda_{ci}\delta/U_b = 4$, and riblet cases with $\lambda_{ci}\delta/U_b = 8$ at (b) $\Lambda/\delta = 0.25$, (c) $\Lambda/\delta = 0.5$, (d) $\Lambda/\delta = 1$, and (e) $\Lambda/\delta = 1.5$ for the lower half channel. Only the results for the half width of the computational domain in the spanwise direction are presented for simplicity. The iso-surfaces are colored by the instantaneous streamwise vorticity ω_1; the red/blue colors indicate the positive/negative values of ω_1.

plane-averaged ($\langle v_a \rangle$) and wake level ($\langle v_d \rangle$) as well as their interaction ($\langle v_i \rangle$), respectively; $C_{D,k}$ splits into $C_{D,ks}$ and $C_{D,kw}$, arising from the shear component P_{ks} and wake component P_{kw} of the TKE production, respectively. Since the energy generated by the TKE production is ultimately transformed into heat via turbulent dissipation, Eq. (12) can be regarded as the relation between the drag coefficient and the energy dissipation.

The components of $C_{D,v}$ for all the cases are presented in Fig. 11(b). For the baseline case, $C_{D,vd}$ and $C_{D,vi}$ are expected to be zero. In comparison with the baseline case, $C_{D,vd}$ makes the dominant contribution to the drag increment for all the riblet cases, while $C_{D,va}$ and $C_{D,vi}$ have much less influence. It is worth noticing that $C_{D,va}$ follows the same variation as Γ's as a function of Λ.

The contours of the wake component of the viscous dissipation [v_d, defined in Eq. (15)] in the cross-stream plane are presented in Fig. 12. For the riblet cases, the intensity of v_d is significantly increased in the vicinity of the riblet grooves with the peak obtained around the riblet crests. This indicates that a significantly increased dissipation of the mean kinetic energy into heat occurs nearby. The increased v_d is mainly observed near the DL, resulting from the high shear stress caused by the downwelling. As the wavelength increases from $\Lambda/\delta = 0.25$ to $\Lambda/\delta = 1$, the intensity of the downwelling around DL (see Fig. 6) and the resultant v_d tend to increase (see Fig. 12). Figure 12(f) presents the vertical profiles of v_d with its magnitude averaged in the wall-normal plane. As Λ varies, the intensity of v_d [see Fig. 12(f)] and the resultant $C_{D,vd}$ [see Fig. 11(b)] for the riblet cases follow the same

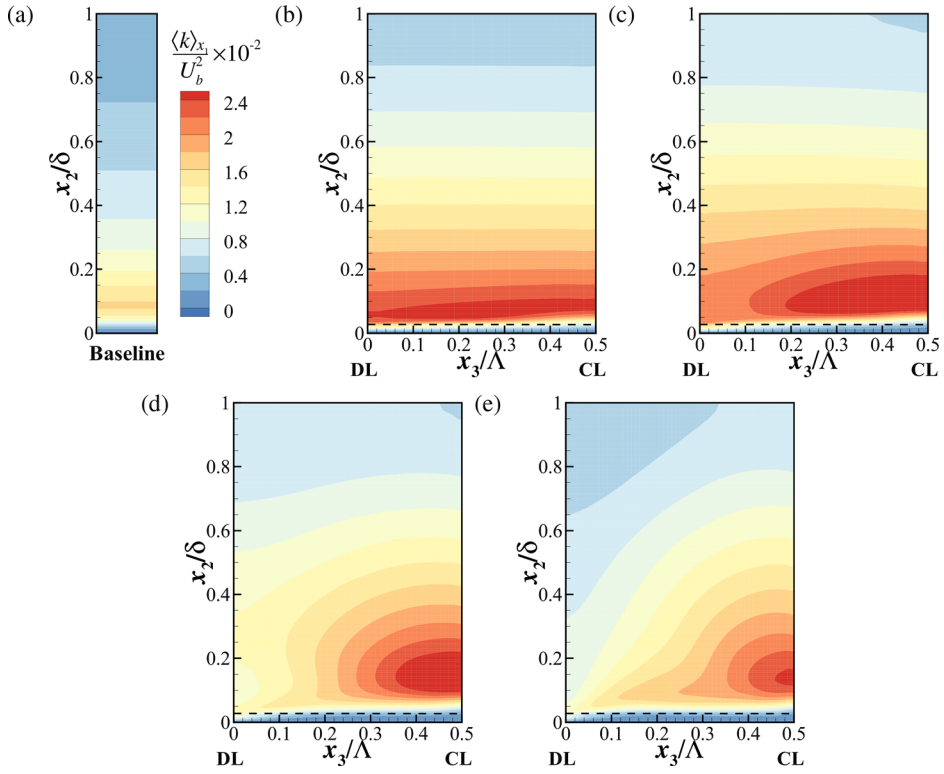

FIG. 10. Contours of turbulence kinetic energy k in cross-stream planes for (a) baseline case and riblet cases with (b) $\Lambda/\delta = 0.25$, (c) $\Lambda/\delta = 0.5$, (d) $\Lambda/\delta = 1$, and (e) $\Lambda/\delta = 1.5$. The dashed line denotes the vertical position of riblet crest.

variation trend with that of Γ, peaking at $\Lambda/\delta = 1$. With a closer examination of the region with high v_d in Fig. 12, it is found that as Λ increases, the region becomes narrower in the spanwise direction. This can be explained from Fig. 6. For the riblet cases at $\Lambda/\delta = 0.25$ and $\Lambda/\delta = 0.5$, a downward motion around the riblet crests is observed from $x_3/\Lambda = 0$ (DL) to $x_3/\Lambda = 0.25$ (middle of DL and CL). In contrast, at $\Lambda/\delta = 1.5$, the downward motion around the riblet crests only occurs from the DL to $x_3/\Lambda = 0.1$. Consequently, with the increase in Λ, the non-negligible regions with high v_d caused by the downwelling become narrower around the DL in the spanwise direction.

The components of $C_{D,k}$ for all the cases are presented in Fig. 11(c). In comparison with the baseline case, both $C_{D,ks}$ and $C_{D,kw}$ for the riblet cases are significantly increased. $C_{D,ks}$ results from the shear production of TKE, P_{ks}, caused by the Reynolds shear stress $-\overline{u_1' u_2'}$. Figure 13 displays the contours of $-\overline{u_1' u_2'}$ in cross-stream planes for all cases. For the riblet cases at $\Lambda/\delta = 0.25$ and

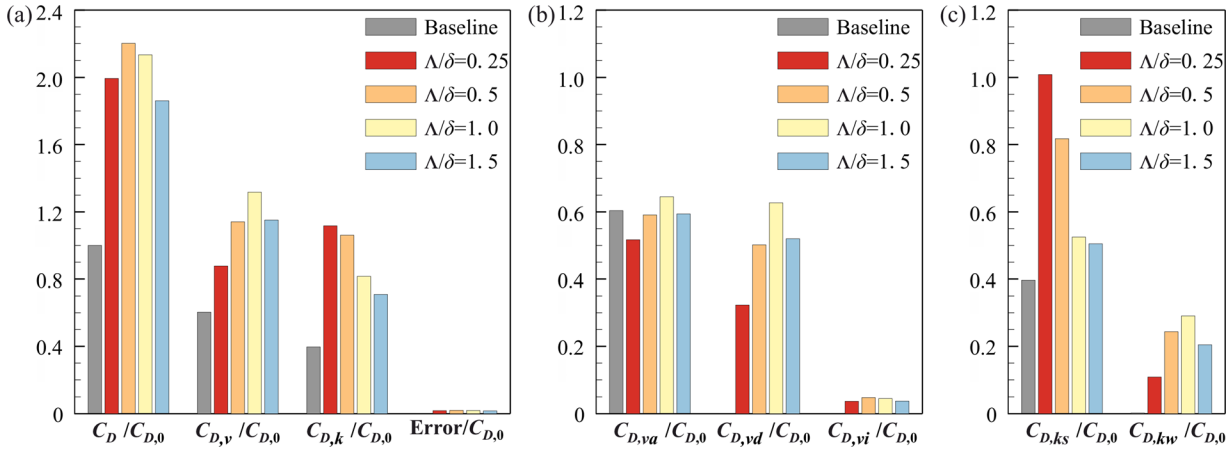

FIG. 11. (a) The drag coefficient C_D and its decomposition terms defined in Eq. (12). Further decomposition of (b) $C_{D,v}$ and (c) $C_{D,k}$ defined in Eq. (15). Each term is normalized by $C_{D,0}$, the drag coefficient of the baseline case.

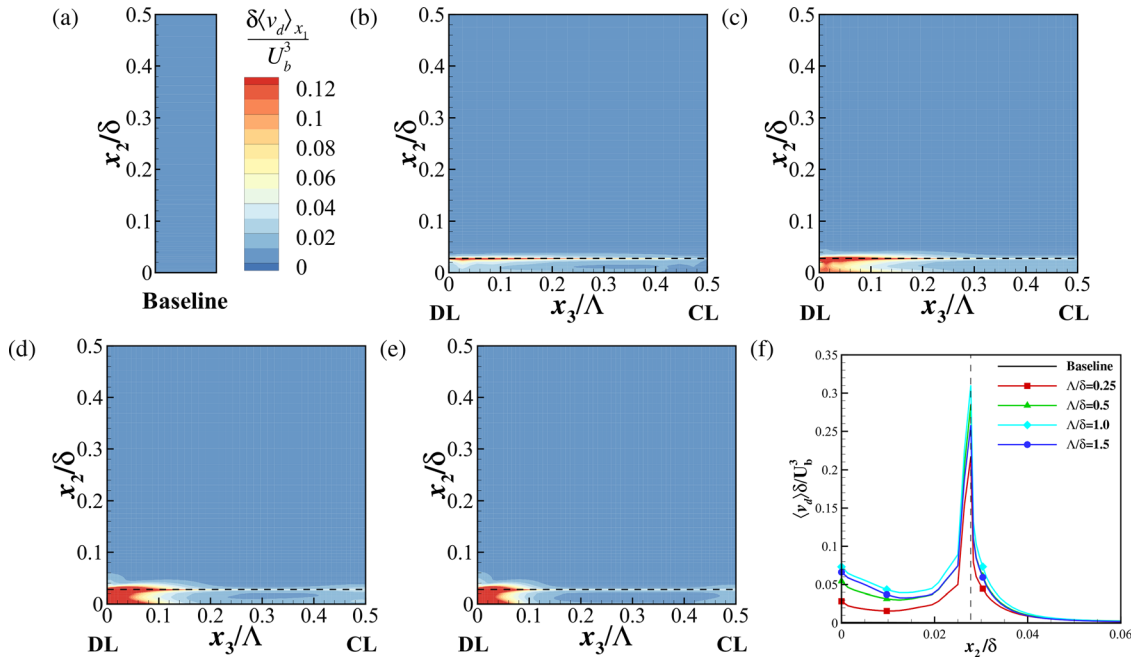

FIG. 12. Contours of viscous dissipation at the wake level v_d in cross-stream planes for (a) baseline case and riblet cases at (b) $\Lambda/\delta = 0.25$, (c) $\Lambda/\delta = 0.5$, (d) $\Lambda/\delta = 1$, and (e) $\Lambda/\delta = 1.5$. (f) Profile of wall-normal plane-averaged viscous dissipation that is related to the dispersive velocity. The dashed line denotes the vertical position of the riblet crest.

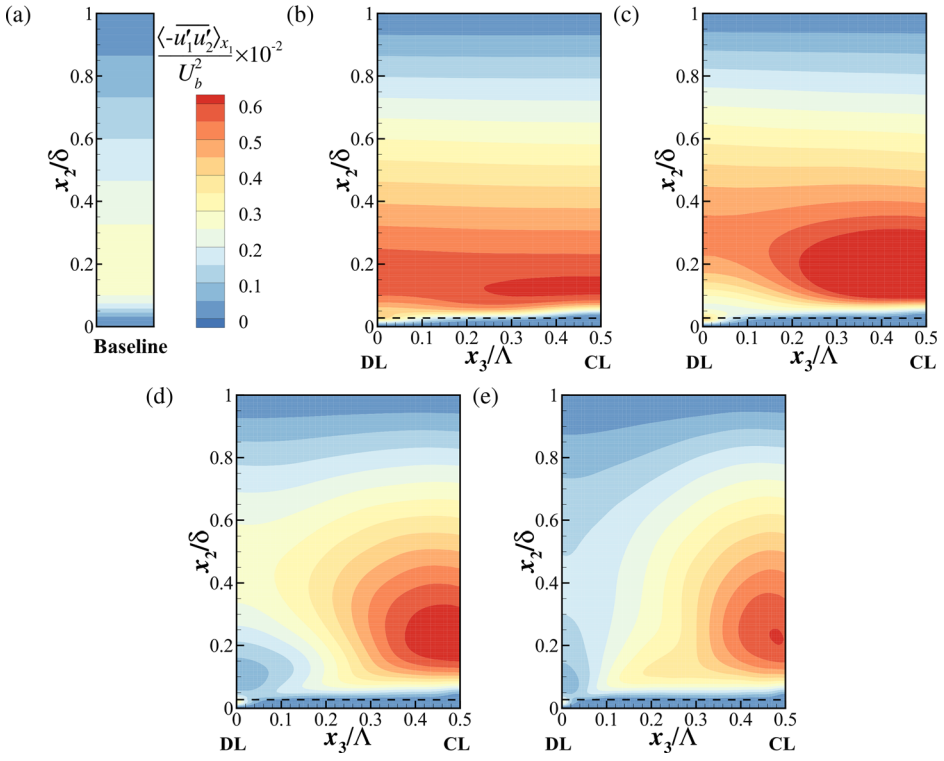

FIG. 13. Contours of Reynolds shear stress $-\overline{u_1'u_2'}$ in cross-stream planes for (a) baseline case and riblet cases with (b) $\Lambda/\delta = 0.25$, (c) $\Lambda/\delta = 0.5$, (d) $\Lambda/\delta = 1$, and (e) $\Lambda/\delta = 1.5$. The dashed line denotes the vertical position of the riblet crest.

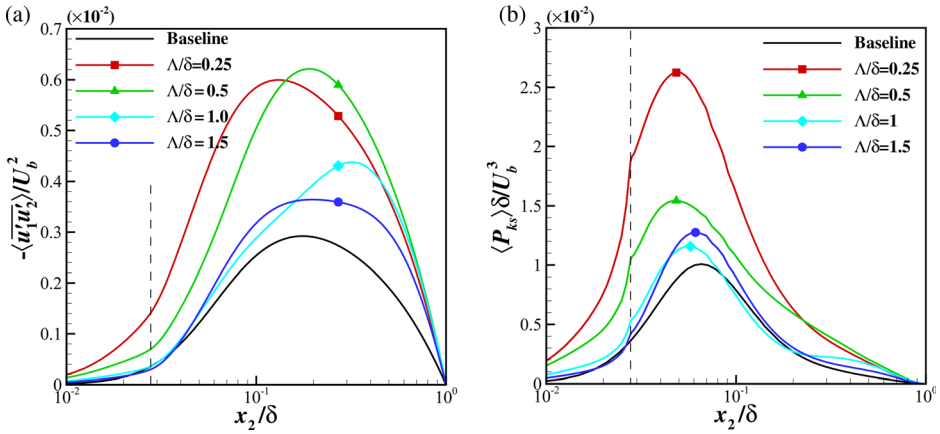

FIG. 14. Profile of wall-normal plane-averaged (a) Reynolds shear stress $\langle -\overline{u_1'u_2'}\rangle$ and (b) shear production of TKE, P_{ks}, for the baseline case and riblet cases. Each term is normalized by U_b^3/δ.

$\Lambda/\delta = 0.5$, the intensity of $-\overline{u_1'u_2'}$ is significantly increased across the span in comparison with the baseline case. This is in agreement with the large number of turbulent structures (see Fig. 9). As a result, the intensity of $-\overline{u_1'u_2'}$ and the resultant P_{ks} is significantly increased, as seen in Fig. 14. In comparison, P_{ks} at $\Lambda/\delta = 0.25$ is much larger than that at $\Lambda/\delta = 0.5$ below $x_2/\delta = 0.2$, owing to the larger $-\overline{u_1'u_2'}$ at $x_2/\delta < 0.1$ [see Fig. 14(a)] and larger shear stress at $0.1 < x_2/\delta < 0.2$ [see Fig. 8(c)]. Above $x_2/\delta = 0.2$, P_{ks} at $\Lambda/\delta = 0.5$ is slightly larger, resulting from the larger $-\overline{u_1'u_2'}$ [see Fig. 14(a)].

For riblet cases at $\Lambda/\delta = 1$ and $\Lambda/\delta = 1.5$, some heterogeneity is observed in the spanwise direction, for $-\overline{u_1'u_2'}$. This is caused by the downwelling/upwelling induced by the large-scale secondary flow motion, which size and intensity is much larger than that at $\Lambda/\delta = 0.25$ and $\Lambda/\delta = 0.5$. Around the DL, $-\overline{u_1'u_2'}$ decreases slightly below $x_2/\delta < 0.4$, while near the CL $-\overline{u_1'u_2'}$ is significantly increased, resulting from the accumulation of near-wall turbulence-rich fluid and upward motion, which is consistent with the instantaneous turbulent structures observed (see Fig. 9). It can be seen from Fig. 14 that $-\overline{u_1'u_2'}$ and the resultant P_{ks} at $\Lambda/\delta = 1$ are slightly larger than that at $\Lambda/\delta = 1.5$, except for the region around $x_2/\delta = 0.1$, owing to the increased $-\overline{u_1'u_2'}$ near $x_3/\Lambda = 0.15$ caused by the local upward motion (see Fig. 6). For the riblet cases, P_{ks} and the resultant $C_{D,ks}$ show a decreasing trend as the wavelength increases.

$C_{D,kw}$ results from the wake component of TKE (P_{kw}), and for the baseline case, its value is zero. For all the riblet cases, P_{kw} is positive and is a non-negligible contribution to the total TKE production, its intensity being comparable to that of P_{ks}, as seen in Fig. 15(a). In the near wall region at $x_2/\delta < 0.02$, the riblet case with the smallest wavelength tends to induce the largest intensity of P_{kw}. Along the wall-normal direction, P_{kw} at $\Lambda/\delta = 0.25$ and 0.5 tends to decrease rapidly and becomes zero at $x_2/\delta > 0.3$. In contrast, P_{kw} at $\Lambda/\delta = 1$ and 1.5 is non-negligible across the channel. It is consistent with the size of the large-scale roll mode (see Fig. 6). This differs significantly from that observed for homogeneous roughness pattern[39,40] where P_{kw} is confined in the near wall region around the roughness crests, its intensity being much smaller than P_{ks}. This can be attributed to the induced large-scale secondary flow that has an influence on the entire flow field. Figure 11(c) shows that the drag component $C_{D,kw}$ arising from P_{kw} follows the same variation trend as that of Γ when Λ varies, making a significant contribution to the total drag increase.

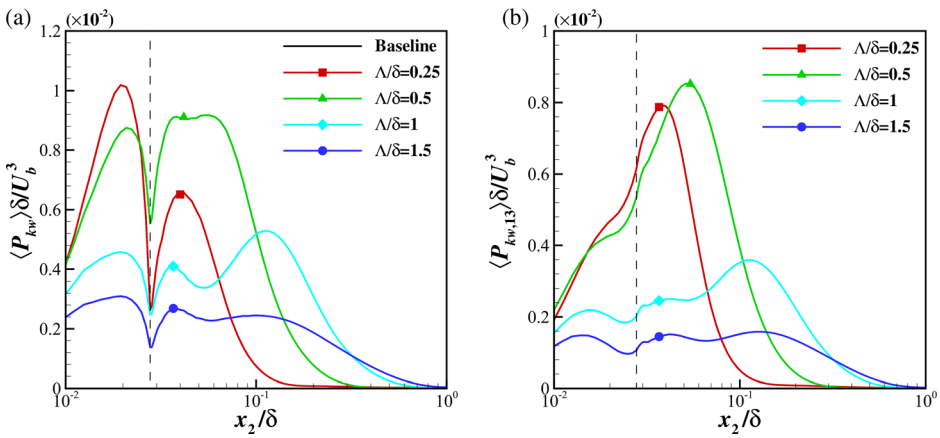

FIG. 15. Profile of the wall-normal plane-averaged (a) P_{kw} and (b) its component $P_{kw,13} = -\overline{u_1'u_3'}\partial\tilde{u}_1/\partial x_3$ for the baseline case and riblet cases. Each term is normalized by U_b^3/δ.

$P_{kw} = -\overline{u_i'u_j'}\frac{\partial \tilde{\bar{u}}_i}{\partial x_j}$ is the sum of nine components, which are the products of the Reynolds stresses $-\overline{u_i'u_j'}$ and the corresponding dispersive velocity gradients $\frac{\partial \tilde{\bar{u}}_i}{\partial x_j}$. $P_{kw,13}$ denotes one component of P_{kw} caused by $-\overline{u_1'u'_3}\frac{\partial \tilde{\bar{u}}_1}{\partial x_3}$. It can be seen from Fig. 15(b) that $P_{kw,13}$ is the dominant term of P_{kw} in the outer region, resulting from the spanwise gradient of the streamwise velocity induced by the large-scale secondary flow. As a result, the intensity of P_{kw} in the outer region follows the same variation trend as Γ when the wavelength varies. This is also the reason why at $\Lambda/\delta = 0.25$, P_{kw} reduces to zero when $x_2/\delta > 0.1$. At $x_2/\delta > 0.3$, $P_{kw,13}$ for the riblet case with $\Lambda/\delta = 1.5$ is slightly larger than that at $\Lambda/\delta = 1$. This is attributed to the larger size of the roll mode, which has a more profound influence in the far field region (see Fig. 6).

In summary, the C–D riblets lead to a significant drag increase, the maximum drag being observed at $\Lambda/\delta = 0.5$. From the proposed drag decomposition method, it is found that the drag increase is dominated by the shear and wake components of the TKE production as well as the wake component of the viscous dissipation. While the drag contribution from the shear component of the TKE production shows a decreasing trend as the wavelength increases, the drag increase caused by the wake component of both the TKE production and viscous dissipation follows the same variation trend as the intensity of the secondary flow.

D. An alternative expression for the drag decomposition from the work point of view

Within the framework of the double averaging defined in Eq. (2), the total kinetic energy averaged in the wall-parallel plane can be divided into three components:

$$\frac{1}{2}\langle \overline{u_i}\overline{u_i}\rangle = \frac{1}{2}\langle \overline{u_i}\rangle\langle \overline{u_i}\rangle + \frac{1}{2}\langle \tilde{\bar{u}}_i\tilde{\bar{u}}_i\rangle + \frac{1}{2}\langle \overline{u_i'u_i'}\rangle, \tag{16}$$

where the second term of the right-hand side is the wake kinetic energy (WKE).[39–41] Multiplying Eq. (4) by $\tilde{\bar{u}}_i$ and rearranging some terms, the transport equation for the WKE per unit mass $\tilde{K} \equiv \tilde{\bar{u}}_i\tilde{\bar{u}}_i/2$ reads

$$\frac{\partial}{\partial x_j}\left[\tilde{K}\bar{u}_j + \frac{\bar{u}_j\bar{p}}{\rho} + \tilde{\bar{u}}_i\overline{u_i'u_j'}\right] = -\tilde{\bar{u}}_i\bar{u}_j\frac{\partial\langle\bar{u}_i\rangle}{\partial x_j} + \frac{\langle\bar{u}_i\rangle}{\rho}\frac{\partial\bar{p}}{\partial x_i} + \nu\tilde{\bar{u}}_i\frac{\partial^2\bar{u}_i}{\partial x_j\partial x_j} + \overline{u_i'u_j'}\frac{\partial\tilde{\bar{u}}_i}{\partial x_j}. \tag{17}$$

Integrating Eq. (17) across the fluid domain with the aid of the Gauss's Theorem, the following energy balance equation can be obtained:

$$\int_0^{2\delta}\phi\left[\underbrace{\langle-\tilde{\bar{u}}_1\tilde{\bar{u}}_2\rangle\frac{\partial\langle\bar{u}_1\rangle}{\partial x_2}}_{\langle P_{ws}\rangle} + \underbrace{\left\langle\overline{u_i'u_j'}\frac{\partial\tilde{\bar{u}}_i}{\partial x_j}\right\rangle}_{\langle -P_{kw}\rangle} + \underbrace{\frac{\langle\bar{u}_1\rangle}{\rho}\left\langle\frac{\partial\bar{p}}{\partial x_1}\right\rangle}_{\langle P_{wp}\rangle} + \underbrace{\nu\left\langle\frac{\partial^2\tilde{K}}{\partial x_jx_j}\right\rangle}_{\langle D_w\rangle} \underbrace{-\nu\left\langle\frac{\partial\tilde{\bar{u}}_i}{\partial x_j}\frac{\partial\tilde{\bar{u}}_i}{\partial x_j}\right\rangle}_{-\langle\nu_d\rangle}\right]dx_2 = 0, \tag{18}$$

where Eq. (3) is applied; the terms from left to right are the shear production P_{ws}, wake production $-P_{kw}$, work by the pressure P_{wp}, and the viscous diffusion D_w and dissipation $-\nu_d$ at the wake level, respectively.

P_{kw} appears in the production term of both the TKE and WKE but with opposite signs, as seen in Eqs. (15) and (18). P_{kw} represents the net transfer between the TKE and WKE, resulting from their interactions.[40,41] Figure 15 shows that P_{kw} is positive for all the riblet cases. As a result, a part of the energy achieved by shear production and pressure work of WKE is dissipated into internal energy by viscous diffusion/dissipation at the wake level; the other part is converted into TKE via P_{kw}, which is ultimately transformed into heat via turbulent dissipation.

Substituting Eq. (18) into Eq. (15) gives the expression for the drag coefficient based on work as

$$C_D = \underbrace{\frac{2}{U_b^3}\int_0^\delta -\phi\nu\langle\bar{u}_1\rangle\left\langle\frac{\partial^2\bar{u}_1}{\partial x_j\partial x_j}\right\rangle dx_2}_{C_{D,vf}} + \underbrace{\frac{2}{U_b^3}\int_0^\delta\frac{\phi\langle\bar{u}_1\rangle}{\rho}\left\langle\frac{\partial\bar{p}}{\partial x_1}\right\rangle dx_2}_{C_{D,wp}} + \underbrace{\frac{2}{U_b^3}\int_0^\delta\phi\langle-\overline{u_1'u_2'}\rangle\frac{\partial\langle\bar{u}_1\rangle}{\partial x_2}dx_2}_{C_{D,ks}} + \underbrace{\frac{2}{U_b^3}\int_0^\delta\phi\langle-\tilde{\bar{u}}_1\tilde{\bar{u}}_2\rangle\frac{\partial\langle\bar{u}_1\rangle}{\partial x_2}dx_2}_{C_{D,ws}}, \tag{19}$$

where the four components denote the drag contribution from the work by the wall-normal plane-averaged viscous force, pressure, Reynolds shear stress, and dispersive stress, respectively. The following expression is applied:

$$\begin{aligned}
&\int_0^\delta -\phi\nu\langle\bar{u}_1\rangle\left\langle\frac{\partial^2\bar{u}_1}{\partial x_j\partial x_j}\right\rangle dx_2 \\
&= \int_0^\delta -\phi\nu\langle\bar{u}_i\rangle\left\langle\frac{\partial^2\bar{u}_i}{\partial x_j\partial x_j}\right\rangle dx_2 = \int_0^\delta -\phi\nu\left\langle\left(\bar{u}_i - \tilde{\bar{u}}_i\right)\frac{\partial^2\bar{u}_i}{\partial x_j\partial x_j}\right\rangle dx_2 \\
&= \int_0^\delta \phi\nu\left(-\left\langle\frac{\partial}{\partial x_j}\left(\bar{u}_i\frac{\partial\bar{u}_i}{\partial x_j}\right)\right\rangle + \left\langle\frac{\partial\bar{u}_1}{\partial x_2}\frac{\partial\bar{u}_1}{\partial x_2}\right\rangle\right. \\
&\quad \left.+\left\langle\frac{\partial}{\partial x_j}\left(\tilde{\bar{u}}_i\frac{\partial\tilde{\bar{u}}_i}{\partial x_j}\right)\right\rangle - \left\langle\frac{\partial\tilde{\bar{u}}_1}{\partial x_2}\frac{\partial\tilde{\bar{u}}_1}{\partial x_2}\right\rangle\right)dx_2 \\
&= \int_0^\delta \phi\nu\left(\frac{\partial\langle\bar{u}_1\rangle}{\partial x_2}\frac{\partial\langle\bar{u}_1\rangle}{\partial x_2} + 2\frac{\partial\langle\bar{u}_1\rangle}{\partial x_2}\left\langle\frac{\partial\tilde{\bar{u}}_1}{\partial x_2}\right\rangle + \left\langle\frac{\partial^2\tilde{K}}{\partial x_jx_j}\right\rangle\right)dx_2.
\end{aligned} \tag{20}$$

The contributions of each component of the total drag coefficient, defined in Eq. (19), are presented in Fig. 16. In comparison with the baseline case, each component for the C–D riblet cases is larger than that of the baseline case. From Eq. (20), $C_{D,vf}$ can be subdivided into three components, the former two terms being related to $C_{D,va}$ and $C_{D,vi}$ defined in Eq. (15). Comparing $C_{D,va}$ in Fig. 11 and $C_{D,vf}$ in Fig. 16 shows that $C_{D,va}$ is the main part of $C_{D,vf}$. They also show the same evolution when the wavelength varies. $C_{D,wp}$ is related to the work by the pressure P_{wp}, and for the baseline case, $C_{D,wp}$ is zero. For all the riblet cases, P_{wp} contributes to the increase in the total drag, and the resultant drag increase is similar for each case.

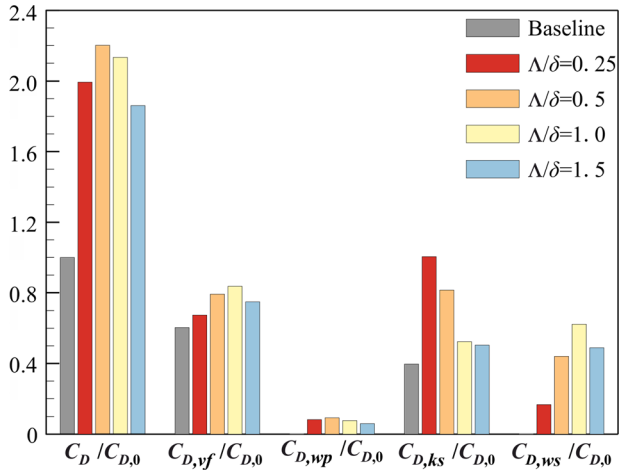

FIG. 16. The drag coefficient C_D and its decomposition terms defined in Eq. (19). Each term is normalized by $C_{D,0}$, the drag coefficient of the baseline case.

Figure 16 shows that the drag increase for the riblet cases is dominated by $C_{D,ks}$ and $C_{D,ws}$. $C_{D,ks}$ comes from the shear production of the TKE and has been analyzed in Sec. IV D. $C_{D,ws}$ comes from the shear production of the WKE (P_{ws}) caused by the dispersive stress $-\tilde{\bar{u}}_1\tilde{\bar{u}}_2$. For the baseline case, $-\tilde{\bar{u}}_1\tilde{\bar{u}}_2$ and the resultant $C_{D,ws}$ are zero. Figure 17 shows the contours of the dispersive stress $-\tilde{\bar{u}}_1\tilde{\bar{u}}_2$ in the cross-stream plane. For the riblet case at $\Lambda/\delta = 0.25$, $-\tilde{\bar{u}}_1\tilde{\bar{u}}_2$ is only noticeable in the near wall region. With the wavelength increase, the region with non-negligible dispersive stress increases in size, resulting from the increased size and intensity of the large-scale roll mode (see Fig. 6). At $\Lambda/\delta = 1.5$, the region with high $-\tilde{\bar{u}}_1\tilde{\bar{u}}_2$ extends to 40% of the half channel height δ despite the small riblet height equal to $h = 2.8\%\delta$. It is also worth noticing that the intensity of $-\tilde{\bar{u}}_1\tilde{\bar{u}}_2$ is comparable to that of the Reynolds shear stress $-\overline{u_1'u_2'}$, as seen in Figs. 14(a) and 18(a). The profile of $-\tilde{\bar{u}}_1\tilde{\bar{u}}_2$ and P_{ws} over the C–D riblets is clearly different from that over homogeneous roughness patterns where $-\tilde{\bar{u}}_1\tilde{\bar{u}}_2$ and P_{ws} are only noticeable in the vicinity of the rough wall.[39,40,42,43]

For the riblet cases, the same trend in the variation of the intensity of Γ and $-\tilde{\bar{u}}_1\tilde{\bar{u}}_2$ is expected since $-\tilde{\bar{u}}_1\tilde{\bar{u}}_2$ is directly related to the downward and upward motions caused by the large-scale secondary flow [see Figs. 8(b) and 18(a)]. As a result, the intensify of P_{ws} [see Fig. 18(b)] and the resultant $C_{D,ws}$ follow the same trend with that of Γ as the wavelength varies.

In summary, a relation between the drag coefficient and the work is derived, where C_D comes from the contribution of the wall-normal plane-averaged viscous force, pressure, Reynolds shear stress, and dispersive stress, respectively. For the riblet case and a small wavelength ($\Lambda/\delta = 0.25$), the dominant factor for drag augmentation comes from the increased Reynolds shear stress, whereas in the case of a large wavelength ($\Lambda/\delta = 1$ and 1.5), the drag increase is predominantly caused by the induced dispersive stress. At $\Lambda/\delta = 0.5$, both components play an important role in the drag increase, and the resultant C_D exhibits a peak.

V. CONCLUSIONS

In this paper, a drag decomposition method is theoretically derived for flows subject to wall roughness. To illustrate this, the case of a turbulent channel flow at $Re_b = 2800$, based on the half channel height and the bulk velocity, is investigated using direct numerical simulations. The drag coefficient is decomposed into physics-informed contributions from several flow field statistical moments. Flows over C–D riblets with a wavelength of 0.25δ–1.5δ are investigated to understand the relationship between the scales/strength of the secondary flow motions and the drag.

It is found that in comparison with the baseline case, the turbulent kinetic energy and the vortical structures for the riblet cases are greatly increased across the span, especially when $\Lambda/\delta \leq 0.5$. For a small wavelength ($\Lambda/\delta = 0.25$), there is not enough spanwise space to

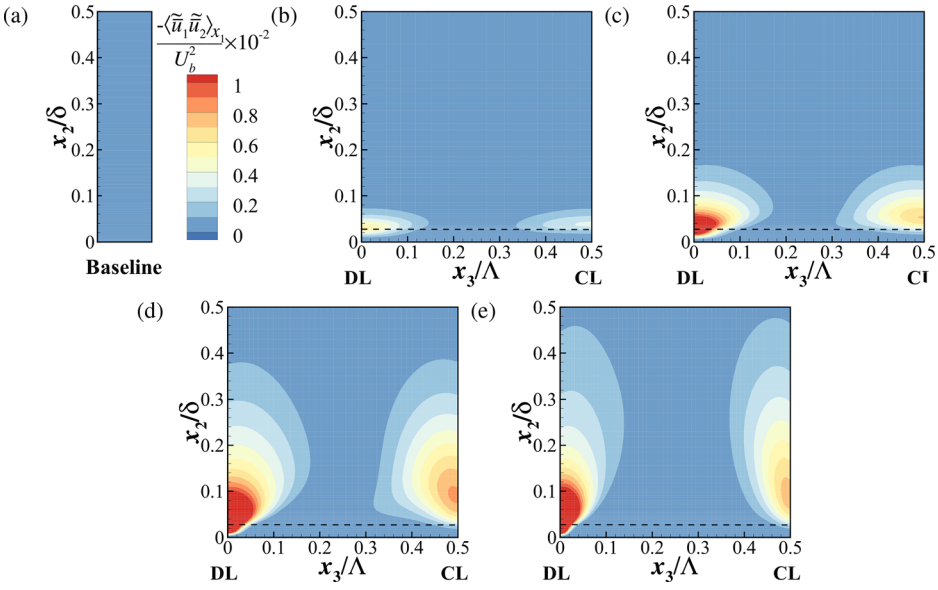

FIG. 17. Contours of dispersive stress $\langle-\tilde{\bar{u}}_1\tilde{\bar{u}}_2\rangle$ in cross-stream planes for (a) baseline case and riblet cases with (b) $\Lambda/\delta = 0.25$, (c) $\Lambda/\delta = 0.5$, (d) $\Lambda/\delta = 1.0$, and (e) $\Lambda/\delta = 1.5$. The dashed line denotes the vertical position of riblet crest.

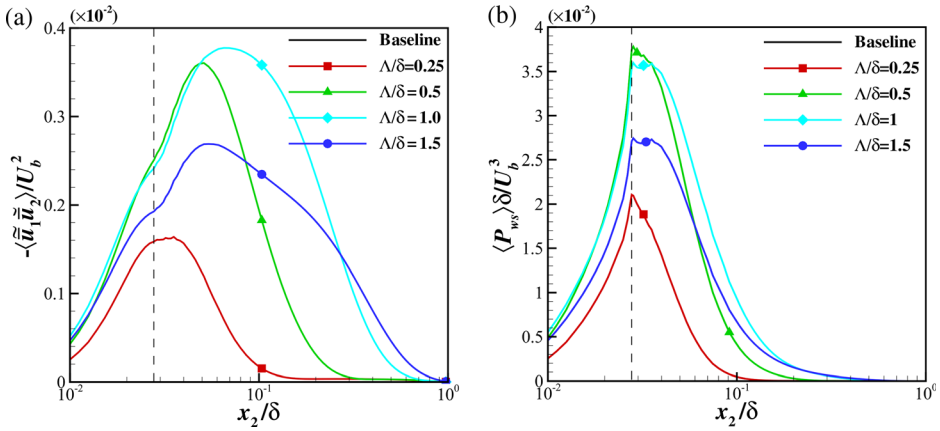

FIG. 18. Profile of the wall-normal plane-averaged (a) dispersive stress $\langle-\tilde{\tilde{u}}_1\tilde{\tilde{u}}_2\rangle$ and (b) shear production of WKE, P_{ws}. The vertical dashed line denotes the position of the riblet crest.

enable the development of the near-wall spanwise velocity, and the resultant intensity of the secondary roll mode is weak. As the wavelength increases, the intensity of the secondary flow motion increases first and then decreases, peaking at $\Lambda/\delta = 1$. When $\Lambda/\delta \geq 1$, some spanwise heterogeneity is observed in the turbulent kinetic energy and the vortical structures, with the strongest enhancement occurring around regions of upwelling.

From the energy dissipation/production point of view, the drag is decomposed into contributions from the viscous dissipation and turbulent production. By using a triple velocity decomposition technique, the former can be subdivided into viscous dissipation at the wall-normal plane-averaged and wake level as well as their interaction. The turbulent production term includes shear and wake components. In all the riblet cases, the drag increase is dominated by the shear and wake components of the turbulent kinetic energy production as well as the wake component of the viscous dissipation. While the drag contribution from the shear component of the turbulent kinetic energy production shows a decreasing trend as the wavelength increases, the drag increase caused by the wake component of both the turbulent kinetic energy production and viscous dissipation follows the same variation trend with the intensity of the secondary flow.

From the work point of view, the drag comes from the work of the wall-normal plane-averaged viscous forces, pressure forces, Reynolds shear stress, and dispersive stress, respectively. For a small wavelength of $\Lambda/\delta = 0.25$, for instance, the dominant factor for the drag augmentation results from the increased Reynolds shear stresses, whereas at large wavelengths ($\Lambda/\delta = 1$ and 1.5), the drag increase is dominated by the dispersive stresses. At $\Lambda/\delta = 0.5$, both components play an important role in the drag increase, and the resultant C_D exhibits a peak.

ACKNOWLEDGMENTS

The first author would like to acknowledge the sponsorship from The China Scholarship Council and The University of Manchester. The authors also gratefully acknowledge support by Newton Fund (No. ST/R006733/1), UK Engineering and Physical Sciences Research Council (EPSRC) through the Computational Science Centre for Research Communities (CoSeC), and the UK Turbulence Consortium (No. EP/R029326/1). The simulations were conducted on HAWK at GCS@HLRS, Germany, and they acknowledge PRACE for awarding us the access.

AUTHOR DECLARATIONS

Conflict of Interest

The authors have no conflicts to disclose.

DATA AVAILABILITY

The data that support the findings of this study are available from the corresponding author upon reasonable request.

REFERENCES

[1]K. Koeltzsch, A. Dinkelacker, and R. Grundmann, "Flow over convergent and divergent wall riblets," Exp. Fluids **33**, 346 (2002).
[2]H. Chen, F. Rao, X. Shang, D. Zhang, and I. Hagiwara, "Flow over bio-inspired 3D herringbone wall riblets," Exp. Fluids **55**, 1698 (2014).
[3]K. Kevin, J. P. Monty, H. Bai, G. Pathikonda, B. Nugroho, J. M. Barros, K. T. Christensen, and N. Hutchins, "Cross-stream stereoscopic particle image velocimetry of a modified turbulent boundary layer over directional surface pattern," J. Fluid Mech. **813**, 412 (2017).
[4]F. Xu, S. Zhong, and S. Zhang, "Statistical analysis of vortical structures in turbulent boundary layer over directional grooved surface pattern with spanwise heterogeneity," Phys. Fluids **31**, 085110 (2019).
[5]K. Kevin, J. Monty, and N. Hutchins, "Turbulent structures in a statistically three-dimensional boundary layer," J. Fluid Mech. **859**, 543 (2019).
[6]T. Guo, S. Zhong, and T. Craft, "Secondary flow in a laminar boundary layer developing over convergent-divergent riblets," Int. J. Heat Fluid Flow **84**, 108598 (2020).
[7]T. Guo, S. Zhong, and T. Craft, "Drag decomposition of laminar channel flows developing over convergent–divergent riblets," Eur. J. Mech.-B/Fluids **92**, 191 (2022).
[8]P. Quan, S. Zhong, Q. Liu, and L. Li, "Attenuation of flow separation using herringbone riblets at M∞ = 5," AIAA J. **57**, 142 (2019).
[9]Q. Liu, S. Zhong, and L. Li, "Effects of bio-inspired micro-scale surface patterns on the profile losses in a linear cascade," J. Turbomach. **141**, 121006 (2019).
[10]B. Nugroho, N. Hutchins, and J. Monty, "Large-scale spanwise periodicity in a turbulent boundary layer induced by highly ordered and directional surface roughness," Int. J. Heat Fluid Flow **41**, 90 (2013).
[11]H. Benschop and W.-P. Breugem, "Drag reduction by herringbone riblet texture in direct numerical simulations of turbulent channel flow," J. Turbul **18**, 717–759 (2017).
[12]T. Guo, S. Zhong, and T. Craft, "Control of laminar flow separation over a backward-facing rounded ramp with C-D riblets—The effects of riblet height, spacing and yaw angle," Int. J. Heat Fluid Flow **85**, 108629 (2020).
[13]A. G. Kravchenko, H. Choi, and P. Moin, "On the relation of near-wall streamwise vortices to wall skin friction in turbulent boundary layers," Phys. Fluids A **5**, 3307 (1993).

[14]M. Yoon, J. Ahn, J. Hwang, and H. J. Sung, "Contribution of velocity-vorticity correlations to the frictional drag in wall-bounded turbulent flows," Phys. Fluids **28**, 081702 (2016).
[15]K. Fukagata, K. Iwamoto, and N. Kasagi, "Contribution of Reynolds stress distribution to the skin friction in wall-bounded flows," Phys. Fluids **14**, L73 (2002).
[16]Y. Kametani and K. Fukagata, "Direct numerical simulation of spatially developing turbulent boundary layers with uniform blowing or suction," J. Fluid Mech. **681**, 154 (2011).
[17]M. Yoon, J. Hwang, J. Lee, H. J. Sung, and J. Kim, "Large-scale motions in a turbulent channel flow with the slip boundary condition," Int. J. Heat Fluid Flow **61**, 96 (2016).
[18]J. Yao, X. Chen, and F. Hussain, "Reynolds number effect on drag control via spanwise wall oscillation in turbulent channel flows," Phys. Fluids **31**, 085108 (2019).
[19]N. Renard and S. Deck, "A theoretical decomposition of mean skin friction generation into physical phenomena across the boundary layer," J. Fluid Mech. **790**, 339 (2016).
[20]W. Li, Y. Fan, D. Modesti, and C. Cheng, "Decomposition of the mean skin-friction drag in compressible turbulent channel flows," J. Fluid Mech. **875**, 101 (2019).
[21]Y. Peet and P. Sagaut, "Theoretical prediction of turbulent skin friction on geometrically complex surfaces," Phys. Fluids **21**, 105105 (2009).
[22]V. Nikora, T. Stoesser, S. M. Cameron, M. Stewart, K. Papadopoulos, P. Ouro, R. McSherry, A. Zampiron, I. Marusic, and R. A. Falconer, "Friction factor decomposition for rough-wall flows: Theoretical background and application to open-channel flows," J. Fluid Mech. **872**, 626 (2019).
[23]W. Ni, L. Lu, C. Ribault, and J. Fang, "Direct numerical simulation of supersonic turbulent boundary layer with spanwise wall oscillation," Energies **9**, 154 (2016).
[24]W. Ni, L. Lu, J. Fang, C. Moulinec, and Y. Yao, "Large-scale streamwise vortices in turbulent channel flow induced by active wall actuations," Flow, Turbul. Combust. **100**, 651 (2018).
[25]W. Ni, L. Lu, J. Fang, C. Moulinec, D. R. Emerson, and Y. Yao, "Flow separation control over a rounded ramp with spanwise alternating wall actuation," Phys. Fluids **31**, 015101 (2019).
[26]J. Fang, F. Gao, C. Moulinec, and D. R. Emerson, "An improved parallel compact scheme for domain-decoupled simulation of turbulence," Int. J. Numer. Methods Fluids **90**, 479 (2019).
[27]V. Nikora, I. McEwan, S. McLean, S. Coleman, D. Pokrajac, and R. Walters, "Double-averaging concept for rough-bed open-channel and overland flows: Theoretical background," J. Hydraul. Eng. **133**, 873 (2007).
[28]C. Vanderwel, A. Stroh, J. Kriegseis, B. Frohnapfel, and B. Ganapathisubramani, "The instantaneous structure of secondary flows in turbulent boundary layers," J. Fluid Mech. **862**, 845 (2019).
[29]T. Medjnoun, C. Vanderwel, and B. Ganapathisubramani, "Effects of heterogeneous surface geometry on secondary flows in turbulent boundary layers," J. Fluid Mech. **886**, A31 (2020).
[30]W. Reynolds and A. Hussain, "The mechanics of an organized wave in turbulent shear flow. Part 3. Theoretical models and comparisons with experiments," J. Fluid Mech. **54**, 263 (1972).
[31]R. D. Moser, J. Kim, and N. N. Mansour, "Direct numerical simulation of turbulent channel flow up to $Re_\tau = 590$," Phys. Fluids **11**, 943 (1999).
[32]F. Xu, S. Zhong, and S. Zhang, "Experimental study on secondary flow in turbulent boundary layer over spanwise heterogeneous microgrooves," Phys. Fluids **32**, 035109 (2020).
[33]C. Vanderwel and B. Ganapathisubramani, "Effects of spanwise spacing on large-scale secondary flows in rough-wall turbulent boundary layers," J. Fluid Mech. **774**, R2 (2015).
[34]D. Chung, J. P. Monty, and N. Hutchins, "Similarity and structure of wall turbulence with lateral wall shear stress variations," J. Fluid Mech. **847**, 591 (2018).
[35]D. D. Wangsawijaya, R. Baidya, D. Chung, I. Marusic, and N. Hutchins, "The effect of spanwise wavelength of surface heterogeneity on turbulent secondary flows," J. Fluid Mech. **894**, A7 (2020).
[36]W. Anderson, J. M. Barros, K. T. Christensen, and A. Awasthi, "Numerical and experimental study of mechanisms responsible for turbulent secondary flows in boundary layer flows over spanwise heterogeneous roughness," J. Fluid Mech. **768**, 316 (2015).
[37]J. Zhou, R. J. Adrian, S. Balachandar, and T. Kendall, "Mechanisms for generating coherent packets of hairpin vortices in channel flow," J. Fluid Mech. **387**, 353 (1999).
[38]J. H. Lee, H. J. Sung, and P.-Å. Krogstad, "Direct numerical simulation of the turbulent boundary layer over a cube-roughened wall," J. Fluid Mech. **669**, 397 (2011).
[39]E. Mignot, E. Barthélemy, and D. Hurther, "Double-averaging analysis and local flow characterization of near-bed turbulence in gravel-bed channel flows," J. Fluid Mech. **618**, 279 (2009).
[40]J. Yuan and U. Piomelli, "Roughness effects on the Reynolds stress budgets in near-wall turbulence," J. Fluid Mech. **760**, R1 (2014).
[41]M. R. Raupach, R. A. Antonia, and S. Rajagopalan, "Rough-wall turbulent boundary layers," Appl. Mech. Rev. **44**, 1–25 (1991).
[42]M. De Marchis, E. Napoli, and V. Armenio, "Turbulence structures over irregular rough surfaces," J. Turbul. **11**, N3 (2010).
[43]P. Forooghi, A. Stroh, P. Schlatter, and B. Frohnapfel, "Direct numerical simulation of flow over dissimilar, randomly distributed roughness elements: A systematic study on the effect of surface morphology on turbulence," Phys. Rev. Fluids **3**, 044605 (2018).